Supporting Information

Angular and Spectral Engineering of Red OLEDs via Cavity-Induced Emission for Photobiomodulation-Related Cellular Responses

Chang Min Lee[1,2,†], Hyun Woo Cho[3,†], Hye-Ryung Choi[4,†], Yeong Beom Kim[1], Geon Lee[1], Mengdi Fu[1], Muhammad Waheed[1], Hyun Jae Lee[1], Insung Ha[1], Keum-Jin Ko[5], Deepak Rajaram Patil[1], P. Justin Jesuraj[6], Chang-Hun Huh[4,*] and Seung Yoon Ryu[1,7,*]

[1]Department of Physics, Dongguk University, Seoul 04620, Republic of Korea

[2]Querrey-Simpson Institute for Bioelectronics, Northwestern University, Evanston, IL, USA

[3]Department of Applied Physics, Korea University Sejong Campus, 2511 Sejong-ro, Sejong City 30019, Republic of Korea

[4]Department of Dermatology, Seoul National University Bundang Hospital, 82 Gumi-Ro 173 Beon-Gil, Seongnam 13620, Korea

[5]Department of Flexible and Printable Electronics, LANL-CBNU Engineering Institute-Korea, Jeonbuk National University, Jeonju 54896, Republic of Korea

[6]Center of Excellence in Materials for Advanced Technologies (CeMAT), Department of Physics and Nanotechnology, SRM Institute of Science and Technology, Kattankulathur, Chengalpattu-603203, India.

[7]Photoenergy Harvesting and Conversion Technology (*phct*), Dongguk University, Seoul 04620, Republic of Korea

[†]C.M. Lee, H.W. Cho and H.-R. Choi contributed equally to this work.

*Authors to whom correspondence should be addressed: chhuh@snu.ac.kr, justie74@dongguk.edu

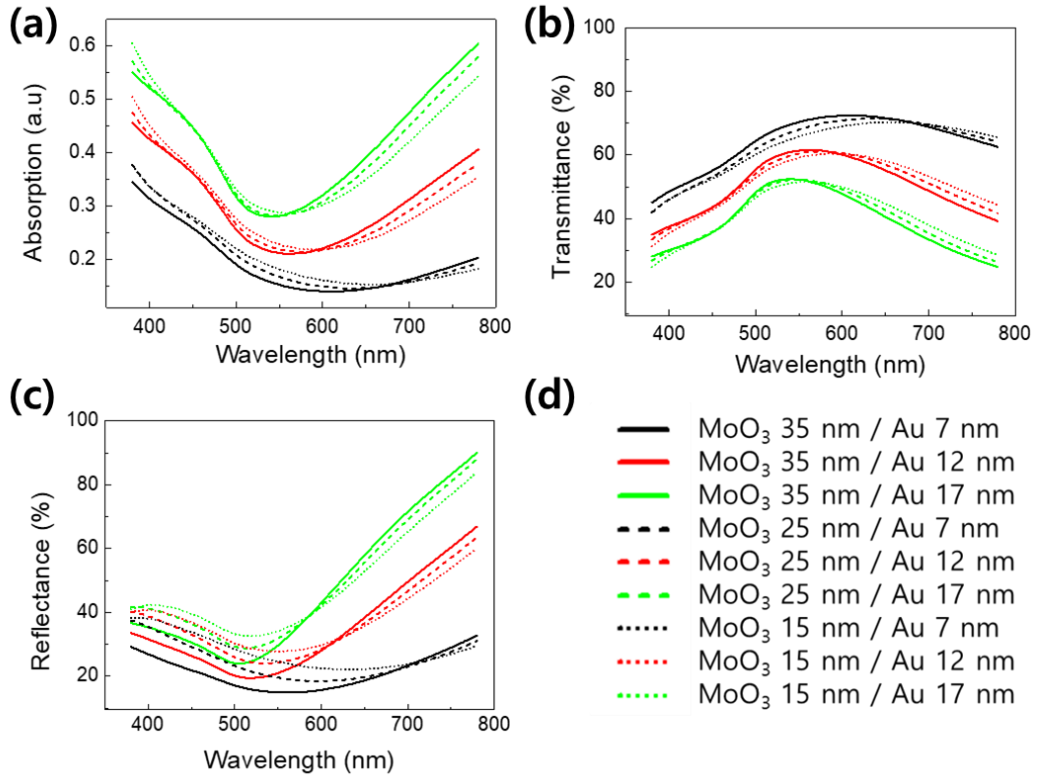


Figure S1. Optical properties of Oxide-Metal-Oxide (OMO) electrodes with varying thicknesses of MoO_3 and Au layers. (a) Absorbance, (b) transmittance, and (c) reflectance spectra of OMO electrodes with different MoO_3 and Au thicknesses. (d) Line-style legend corresponding to the different OMO electrode configurations.

The transmittance, reflectance, and absorbance spectra of OMO electrodes were systematically compared to evaluate their suitability for cavity-type device architectures. While variations in the bottom MoO_3 thickness induced only minor changes in the overall spectral profiles, the Au interlayer thickness played a dominant role in determining the optical characteristics. In particular, increases in Au thickness led to noticeable shifts in both transmittance and reflectance, thereby strongly influencing the cavity resonance conditions. Based on this screening, an optimized electrode configuration employing 15 nm of MoO_3 and 17 nm of Au was selected and used in the final OLED devices to ensure balanced transparency and reflectivity, leading to stable red emission within the therapeutic window.

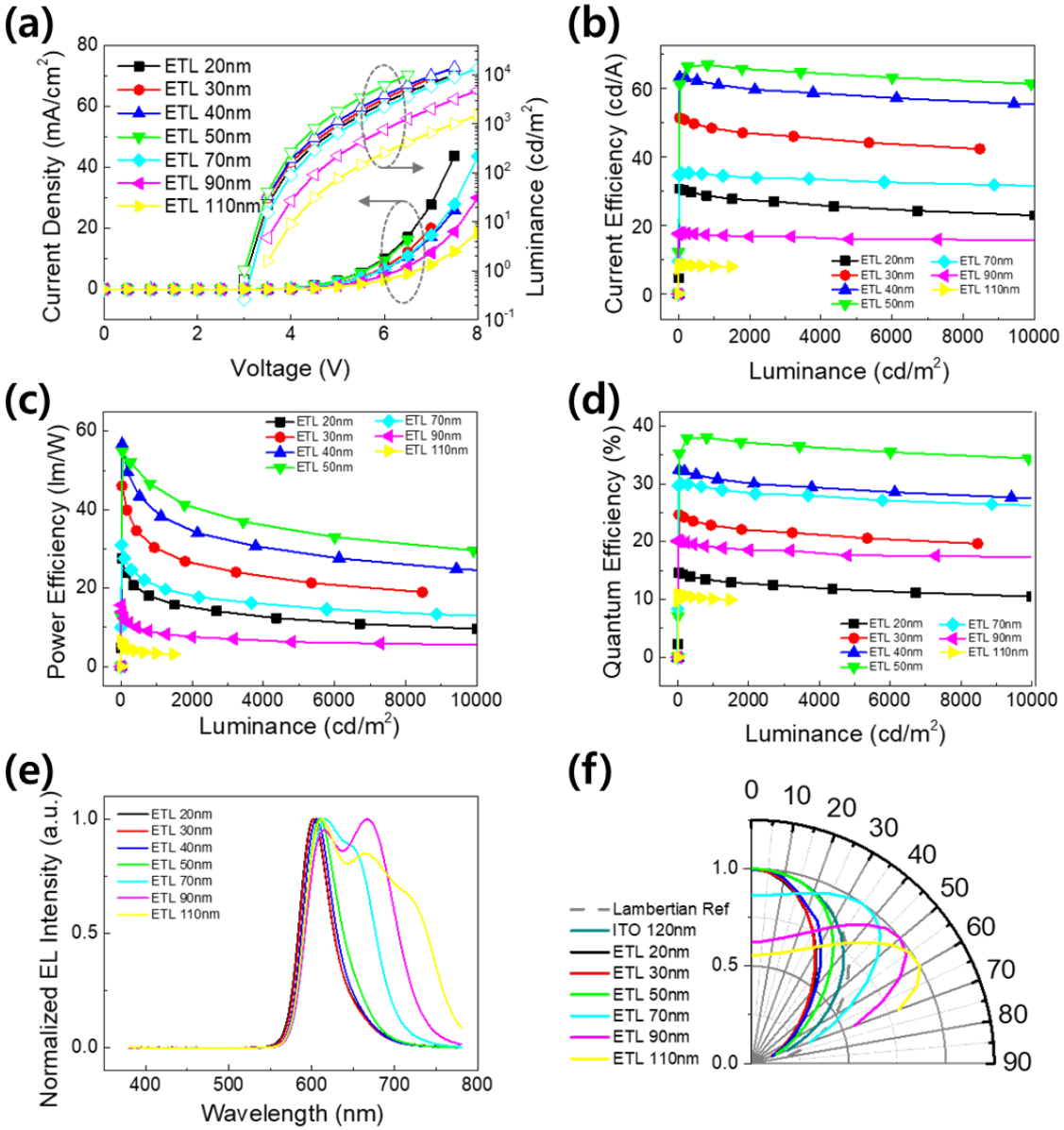


Figure S2. Device performance of red OLEDs with varying ETL thicknesses.

To identify cavity conditions that yield distinct angular emission profiles, the electron transport layer (ETL, TmPyPB) thickness was systematically varied. (a) The J–V–L characteristics, (b) current efficiency, (c) power efficiency, and (d) external quantum efficiency reveal strong dependence on ETL thickness, where the apparent efficiency variations primarily originate from changes in current injection and cavity effects. Since the measurements were performed using a CS-2000 spectroradiometer along the surface normal, devices with different ETL thicknesses exhibited distinct efficiencies and angular distributions rather than intrinsic performance differences. (e) Electroluminescence (EL)

spectra and (f) angular emission plots further demonstrate that ETL thickness critically determines both spectral width and emission distribution. Based on this screening, an ETL thickness of 50 nm was selected to realize the candle-like emission profile, while 70 nm was identified as the optimal thickness for generating the batwing emission profile employed in the main text.

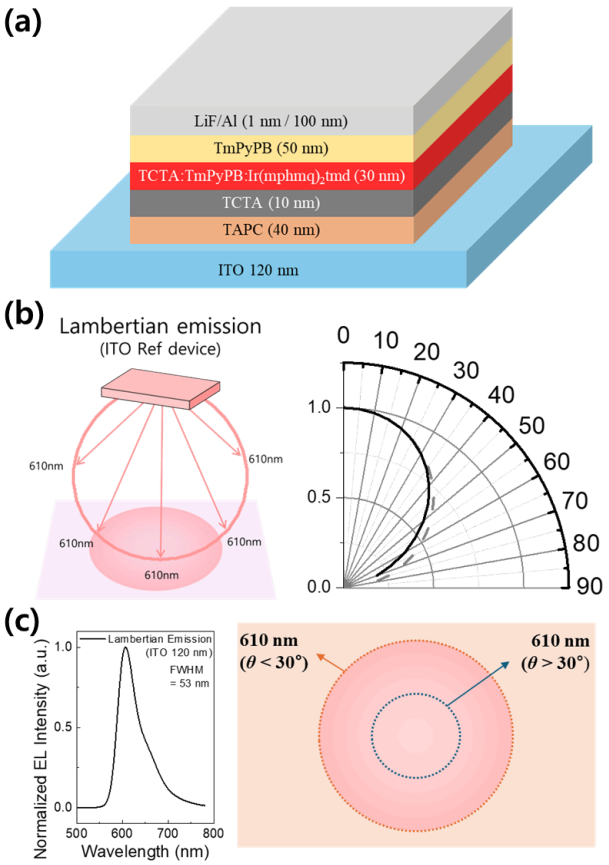


Figure S3. Angular emission and spectral characteristics of the reference ITO-based Lambertian OLED. (a) Device architecture of the ITO-based Lambertian OLED. (b) Schematic illustration of the Lambertian emission profile and the corresponding angular intensity distribution. (c) EL intensity profile and schematic representation of angle-independent emission centered at 610 nm.

Figure S3 shows the structural design and optical properties of the ITO-based Lambertian emission device, which served as the reference condition in our study. The device structure consists of a conventional multilayer stack built on a 120 nm-thick ITO electrode, followed by TAPC (40 nm), TCTA (10 nm), an emissive layer of TCTA:TmPyPB:Ir(mphmq)$_2$tmd (30 nm), an electron transport layer (TmPyPB, 50 nm), and LiF/Al cathodes.

Optically, this configuration generates a Lambertian emission profile, with light intensity distributed uniformly across all angles. The corresponding EL spectrum exhibits a stable peak centered at 610 nm, with negligible angular dependence even at large viewing angles. This angular invariance and spectral stability confirm that the ITO device produces homogeneous irradiance, while maintaining limited spectral modulation.

Within the context of biological testing, the Lambertian device was employed as a reference group to benchmark the performance of cavity-enhanced candle and batwing devices. Its stable but spectrally narrow output enables direct comparison, highlighting how emission engineering in cavity devices introduces angular- and wavelength-dependent variations that influence cellular outcomes.

Section S1. Detailed Calculation Methodology for Radiometric Irradiance

To convert the measured forward luminance (L_0 = 500 cd·m^{-2}) into an estimated radiometric power density (E_e, in mW·cm^{-2}), we considered both the angular emission profiles and the spectral luminous efficacy of each device.[1, 2]

1. Evaluation of Total Luminous Flux Density (M_v)

The total luminous flux density per unit area (M_v, in lm·m^{-2}) emitted into the forward hemisphere is determined by integrating the experimentally measured relative angular intensity distribution,[3, 4] $I_{rel}(\theta)$, as follows (1):

$$M_v = 2\pi L_0 \int_0^{\frac{\pi}{2}} I_{rel}(\theta) \sin sin\,\theta \cos cos\,\theta \; d\theta \qquad (1)$$

,where θ represents the viewing angle relative to the surface normal. For an ideal Lambertian emitter ($I_{rel}(\theta) = 1$), this equation (2) simplifies to:

$$M_{v,Lamb} = \pi L_0 \qquad (2)$$

For the non-Lambertian profiles (candle and batwing emissions), the integration was performed numerically using the experimentally obtained angular emission data.

2. Derivation of Spectral Luminous Efficacy (K)

The spectral luminous efficacy (K, in lm·W^{-1}) of each EL spectrum was calculated using the normalized EL intensity spectrum, $S(\lambda)$, and the CIE 1931 standard photopic luminous efficiency function, $V(\lambda)$, as follows (3):

$$K = K_m \frac{\int_{380}^{780} S(\lambda)V(\lambda)d\lambda}{\int_{380}^{780} S(\lambda)d\lambda} \qquad (3)$$

,where K_m is the maximum spectral luminous efficacy of human photopic vision, mathematically defined as 683 lm·W^{-1} at a wavelength of λ = 555 nm.

3. Final Conversion to Areal Irradiance (E_e)

The total radiometric radiant flux density (M_e, in W·m^{-2}) at the active emitting surface is given by the quotient of M_v and K.[3] To express this value in the practical unit of mW·cm^{-2}, a scaling factor of 0.1 was applied to account for the metric area conversion (1 m^2 = 10,000 cm^2) and the power scaling (1 W = 1,000 mW) (4):

$$E_e = \frac{1000}{10000} \cdot \frac{M_v}{K} = \frac{1}{10} \cdot \frac{M_v}{K} \qquad (4)$$

Using this approach, the estimated radiometric power densities under a fixed forward luminance of 500 cd·m^{-2} were calculated to be 0.511 mW·cm^{-2} for candle-emission device (K = 224.6 lm·W^{-1}), 0.682 mW·cm^{-2} for the Lambertian emission device (K = 220.3 lm·W^{-1}), and 1.114 mW·cm^{-2} for batwing-emission device (K = 165.2 lm·W^{-1}).

These values represent estimated radiometric power densities derived from the measured luminance, angular emission profiles, and EL spectra of the devices. Because the devices exhibit different angular emission characteristics, the calculated values should be interpreted as approximate estimates rather than exact irradiance values delivered to the cell plane.

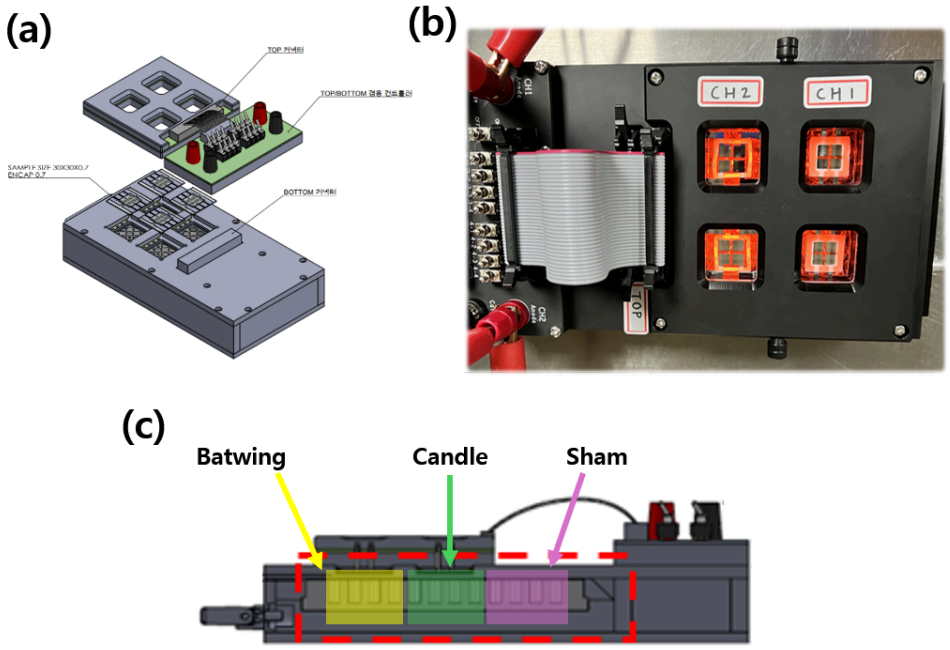


Figure S4. Custom-designed jig for red OLED irradiation experiments.

(a) Schematic illustration of the custom-designed irradiation jig, showing the top and bottom housings with electrical connectors for stable mounting of multiple OLED samples. The jig was designed to maintain consistent geometrical alignment and reproducible irradiation conditions during biological experiments. (b) Photograph of the jig during operation, showing four simultaneously mounted OLED devices under bias. (c) Cross-sectional schematic indicating the relative positions of the batwing-emission, candle-emission, and sham conditions within the same irradiation platform. All groups were processed simultaneously under identical environmental and geometrical conditions, with the only difference being the presence or absence of OLED light exposure. The distance between the OLED surface and the cell layer was maintained at approximately 13 mm for all irradiation conditions.

	Control	ITO	Candle	Batwing
Cell response (OD 450nm)	0.644	0.710	0.759	0.748
	0.649	0.701	0.724	0.805
	0.660	0.703	0.709	0.771
	0.636	0.777	0.714	0.754
	0.638	0.700	0.768	0.825
	0.664	0.721	0.772	0.836
	0.702	0.699	0.735	0.858
	0.656	0.698	0.753	0.756
	0.658	0.792	0.769	0.809
	0.689	0.760	0.728	0.812
Average	0.661	0.726	0.743	0.797
Standard deviation	0.021	0.036	0.024	0.038

Table S1. Raw CCK-8 absorbance data (OD at 450 nm) obtained under different OLED irradiation conditions.

Each column represents individual absorbance values measured from independent samples (n = 10) for the control (sham irradiation), ITO-based Lambertian device, candle-emission device, and batwing-emission device. The average values and standard deviations for each condition are summarized at the bottom of the table.

These data were used to calculate the mean values and error bars presented in **Fig. 5** and for statistical analysis. The batwing-emission device exhibited the highest average OD450 value among the tested conditions, consistent with enhanced cellular metabolic activity under the selected irradiation conditions. One-way ANOVA revealed significant differences among the experimental groups ($F(3, 36) = 34.13$, $p < 0.001$). Post-hoc Tukey's multiple comparison test confirmed a significant difference between the Batwing and Candle groups ($p < 0.01$). No significant difference was observed between the ITO and Candle groups ($p = 0.608$).

Reference

1. Wyszecki, G.; Stiles, W. S., *Color science: concepts and methods, quantitative data and formulae*. John wiley & sons: 2000.
2. Kawabata, T.; Ohno, Y., Optical measurements of OLED panels for lighting applications. *Journal of Modern Optics* **2013,** *60* (14), 1176-1186.
3. Saleh, B. E.; Teich, M. C., *Fundamentals of photonics, 2 volume set*. john Wiley & sons: 2019.
4. Moreno, I.; Sun, C.-C., Modeling the radiation pattern of LEDs. *Optics express* **2008,** *16* (3), 1808-1819.